

# Ridge propagation and the stability of small mid-ocean ridge offsets

Hugh Harper<sup>1</sup>, Karen Luttrell<sup>2</sup>, David T. Sandwell<sup>1</sup>

<sup>1</sup>Scripps Institution of Oceanography, University of California San Diego, La Jolla, CA, USA

<sup>2</sup>Department of Geology and Geophysics, Louisiana State University, Baton Rouge, LA, USA

## Key Points:

- Propagating ridges are rarely observed at ridge offsets greater than 30 km, possibly a result of lithospheric strength.
- We develop a model framework that balances material strength at ridge offsets and forces driving ridge propagation.
- Greater strength of the lithosphere as ridge offset increases may limit ridge propagation.

---

Corresponding author: Hugh Harper, [huharper@ucsd.edu](mailto:huharper@ucsd.edu)

## Abstract

The mid-ocean ridge system comprises a series of spreading ridges, transform faults, propagating ridges, and other non-transform offsets. Transform faults remain stable for millions of years leaving long linear scars, or fracture zones, on older seafloor. Propagating ridges migrate in the ridge parallel direction leaving V-shaped or W-shaped scars on older seafloor. Vertical gravity gradient (VGG) maps can now resolve the details of the ridge segmentation. For slow- and intermediate-spreading ridges, there appears to be an offset length threshold above which adjacent ridges do not propagate so remain as stable transform faults. We propose this threshold is due to the yield strength of the lithosphere, and we develop a model framework based on a force balance wherein forces driving propagation must exceed the integrated shear strength of the offset zone. We apply this model framework to 4 major propagating ridges, 55 seesaw propagating ridges, and 69 transform faults. The model correctly predicts the migration of major propagating ridges and the stability of transform faults, but the results for SSPs are less accurate. Model predictions for direction of ridge propagation are mixed as well. This model framework simplifies deformation in the shear zone, but can possibly explain why non-transform deformation is preferred at short offsets.

## Plain Language Summary

Mid-ocean ridges are constructive plate boundaries where new crust is created. In map view, the system resembles a stair-step configuration of alternating spreading ridges and ridge offsets. Some ridges and offsets, typically large ones, remain fixed and maintain their plan-view shape over many millions of years, while other ridges, usually those bound by shorter offsets, may slowly grow and shrink – such behavior is revealed in maps of the seafloor. The different behavior is possibly due to the material strength of the oceanic crust and upper mantle which, if great, will inhibit ridge growth. To test our hypothesis, we estimate the total material strength at identified ridge offsets and compare this to an estimate of forces contributing to ridge growth. Our estimates can explain why large offsets maintain their shape, and may explain why short offsets do not and allow some segments to grow and shrink.

## 1 Introduction

The global mid-ocean ridge system comprises a series of spreading segments and spreading segment offsets (transform faults and propagating ridges). Ridges and transform faults commonly trend perpendicular and parallel to the direction of spreading, respectively. Why this configuration of ridges and transform faults is so prevalent is an unanswered question of plate tectonics. Lachenbruch and Thompson (1972) proposed that an orthogonal configuration of ridges and transform faults minimizes the forces that resist plate spreading. An implication of this model is that the force resisting plate motion along a transform fault is much less than the resistive force along the spreading boundary – i.e., transforms are weak. Oldenburg and Brune (1975), in analyzing the wax models of Oldenburg and Brune (1972), also conclude the resistive forces along a transform must be less than the shear strength of the solid material. Observations of patterns in seismicity and oblique faulting at the ends of ridge segments suggest variations from the regional stress field which may be the result of weak transform faults. Studies of seismic moment budget (Boettcher & Jordan, 2004) find a cumulative moment release deficit of 85-90% compared to kinematic models, suggesting weak coupling at oceanic transform faults. Shi et al. (2022) showed that seismic activity of many oceanic transform faults is spatially segmented and that variations in fault zone properties (such as coupling) must vary along strike. Morgan and Parmentier (1984) estimated the ratio of normal stress along the ridge to shear stress on the transform fault and found a stress ratio of 3-5 was required to explain observed faulting patterns. Behn et al. (2002) investigated the ef-

fect of oceanic transform faults on the stress state of the lithosphere and found that low values of mechanical coupling (5%) along transform faults best explains the observed faulting patterns near large transforms, consistent with the results of Morgan and Parmentier (1984).

Transform faults tend to remain stable, or stationary with respect to the plate boundary, for long periods of time. Fracture zones, the off-axis traces of transform faults, provide critical information for plate reconstructions of the ocean basins as they trace the small circles of a pole of rotation. The stable ridge-transform-ridge configuration is common where ridge offsets are large. However, for small segment offsets (less than about 30 km), the observed configurations are not so simple. Instead of a transform fault, the offset may appear as an overlapping spreading center (common at fast-spreading ridges) or the more general non-transform offset (common at slow- and intermediate-spreading ridges) (e.g. Carbotte et al., 2016). Grindlay et al. (1991) suggested that, for shorter offsets, the ratio of ridge normal stress to offset shear stress is closer to unity and that coupling may be enhanced at short offsets. Grindlay and Fox (1993) found, for 3 of 5 example offsets, a ridge normal to offset shear stress ratio of 1-3 best explains the observed deformation patterns. Shorter offsets may migrate along the strike of a ridge, accompanied by the lengthening and shortening of the adjacent ridges (the propagating and failing ridges, respectively).

Hey (1977) provides a kinematic model for ridge propagation and identifies some key morphological features such as the outer pseudofault and inner pseudofault/sheared zone complex (Figure 1a). Ridge propagation rates are generally similar to local half-spreading rates (Morgan & Sandwell, 1994) although there are exceptions to this rule (e.g. Kleinrock et al., 1997). There are many non-exclusive driving mechanisms invoked to explain ridge propagation such as: regional topographic gradients (e.g. (Morgan & Sandwell, 1994)); changes in direction of plate motion (e.g. Hey et al., 1980); or changes in magma supply, either hot-spot driven (e.g. Brozena & White, 1990; Hey et al., 2010) or segment-scale variations in magmatic inputs (e.g. Dannowski et al., 2018; Zheng et al., 2019). Ridge propagation models (and ridge segmentation models more generally) may be classified as either tectonic or magmatic. To explain ridge segmentation and propagation patterns, tectonic models suggest tectonic forces as the cause, whereas magmatic models posit mantle melting patterns as the mechanism.

A propagating ridge may propagate uniformly in one direction, or the direction of propagation may reverse over time (the former propagating ridge becomes the failing ridge, vice versa) (Figure 1b). Recently, several studies have documented off-axis scars of propagating ridges in satellite-derived gravity, mostly on seafloor generated at half-spreading rates between 10 and 35 mm/yr (Matthews et al., 2011; Harper et al., 2021). The scars show that the direction of propagation along the ridge often reverses leaving symmetrical “W” patterns in the seafloor. The seesaw patterns are not congruent along nearby seafloor of similar age as could occur if the propagation was driven by minor changes in spreading direction of the two plates. Using satellite-derived gravity measurements, one can examine numerous present-day propagating ridges and the associated ridge offsets (Figure 2). From our previous analysis (Harper et al., 2021), we determine that propagating ridges mostly occur when an offset is less than 30 km (or about 2.5 Myr for the observed range of spreading rates) (Figure 2c). For offset distances greater than 30 km, ridge offsets are almost entirely transform faults and do not migrate. The reason for this threshold offset length is not obvious.

Morgan and Parmentier (1985) suggested that “when a transform fault grows too long, the energy available for propagation will be less than the extra work required to cause transform migration.” The goal of this study is to examine the offset distance threshold that separates transform faults from propagating ridges, which we model as migrating transform fault zones. We define a stable offset to be stationary with respect to a plate boundary, and we hypothesize that the stability of an offset is related its length

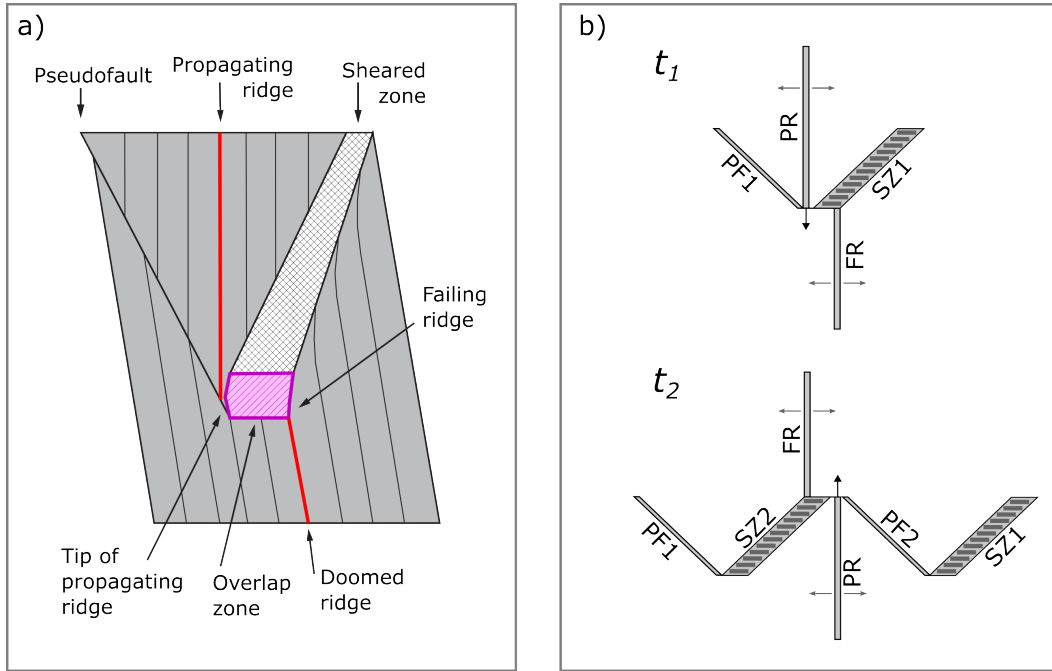


**Figure 1.** (a) Plan view schematic diagram of propagating ridge, modified from Hey (2001), all major features labeled. Spreading axes are colored red. The overlap zone, in pink, is a region of active shearing. (b) Schematic diagram of a “seesaw” propagating ridge showing an epoch of propagation (upper) followed by a reversal and second epoch of propagation (lower). PF = pseudofault, SZ = sheared zone, PR = propagating ridge, FR = failing ridge. Both are examples of migrating ridge offsets.

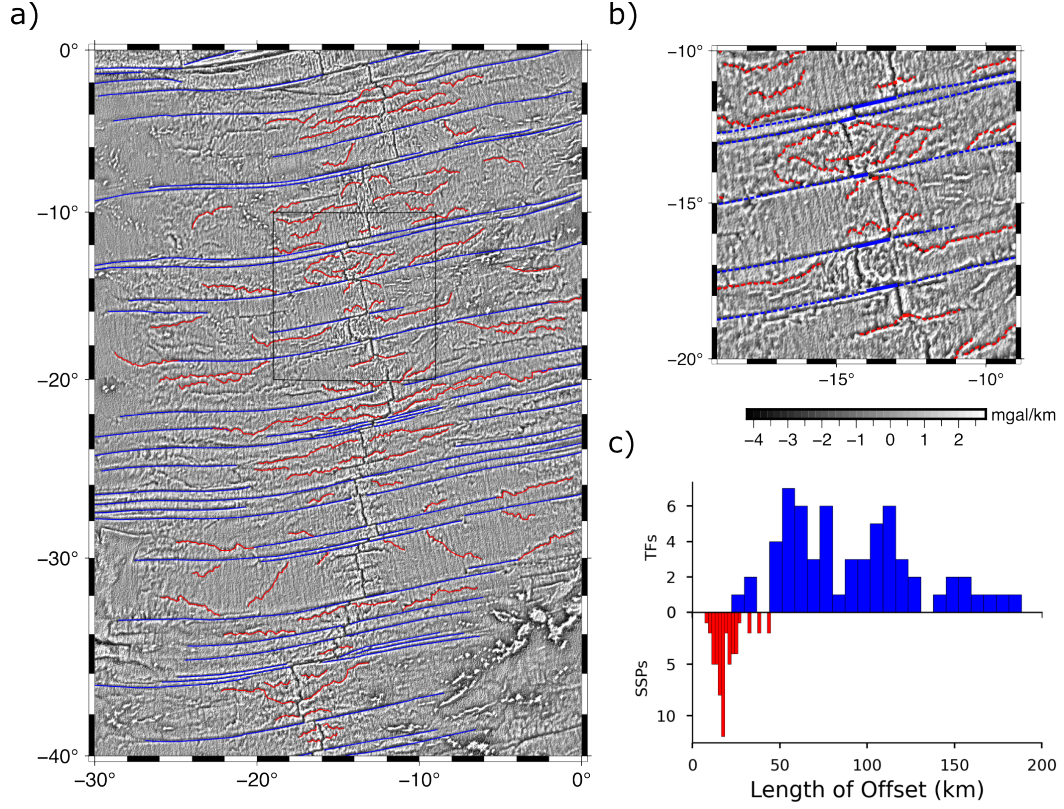


**Figure 2.** (a) Vertical gravity gradient (VGG) map of southern Mid-Atlantic Ridge. Fracture zones (created at ridge transform faults) are highlighted in blue. Seesaw propagators (SSPs) presented in Harper et al. (2021) are shown in red. Box shows region in (b). (b) Zoomed-in view of stable and migrating ridge offsets. Where SSPs can be followed to the spreading ridge, we digitize the present ridge offset. SSP ridge offsets are shown in thicker red pen. Transform fault offsets are shown in thicker blue pen. (c) (after Harper et al., 2021) Measured length of ridge offsets for stable transform faults (upper, blue) and “seesaw” propagators (lower, red).

by the shear stress required to migrate the transform fault (or shear zone) through new lithosphere. We approach this problem with an energy balance model first proposed by Morgan and Parmentier (1985) which we modify to include the energetic effects of a migrating offset. We apply this model to a collection of ridge segments and offsets at slow-to intermediate-spreading ridges to test whether the shear strength of the oceanic lithosphere is a key factor of ridge propagation and offset stability.

## 2 Energy balance of stable and unstable ridges

Morgan and Parmentier (1985) proposed an energy balance for propagating ridges where, for a ridge to propagate, the energy available for propagation must be greater than the energy dissipated due to propagation. The energy balance for a stable spreading ridge with no forces driving propagation can be stated:

$$F dx = \Phi dt, \quad (1)$$

where  $F$  is the force acting on the lithosphere in the spreading direction;  $dx$  is the increment of spreading in the time interval  $dt$ ;  $\Phi$  is the energy dissipation at the spreading segment from both viscous resisting forces at the spreading center and shear resistance along the transform fault (although the latter term will be small as transform faults are known to be weak). In their model, the spreading ridge is treated as a mode 1 fracture, and an additional force driving propagation of the fracture,  $F^*$ , is balanced by additional viscous dissipation,  $\Phi^*$  and decrease in material strain energy from incremental fracture growth. The force driving propagation is from a gravity spreading stress associated with an anomalously shallow ridge axis.

Here, we use the same basic approach of separating the driving forces into two parts – the force  $F$  needed to drive normal ridges and transform faults and an additional force  $F^*$  that drives ridge propagation. However, we do not treat the ridge segments as mode 1 fractures. We propose that the forces driving propagation must at least exceed the integrated shear resistance associated with the ridge offset. If we assume equation 1 is true and the excess force,  $F^*$ , may drive propagation, we have:

$$(F + F^*) dx = (\Phi + \Phi^*) dt \quad (2)$$

$$F^* U = \Phi^*, \quad (3)$$

where  $\Phi^*$  is dissipation associated with ridge propagation and  $U$  is the half spreading rate ( $dx/dt$ ). We will consider migrating the transform fault or zone the primary mechanism of dissipation. The condition that the driving force must at least exceed the shear resistance is then:

$$F^* U \geq \Phi_O^*, \quad (4)$$

where  $\Phi_O^*$  is the offset shear resistance.

For a ridge segment of length  $L_R$ , we have the driving force:

$$F^* = \int_{L_R} F_s dL, \quad (5)$$

where  $F_s$  is the excess force per unit length in the direction of spreading.

When a ridge incrementally propagates, new material enters the transform shear zone (Figure 3a). Within this zone, the material is stressed beyond its yield strength, so the total resistance of shearing the offset zone is:

$$\Phi_O^* = 2U \int_{L_O} S dL. \quad (6)$$

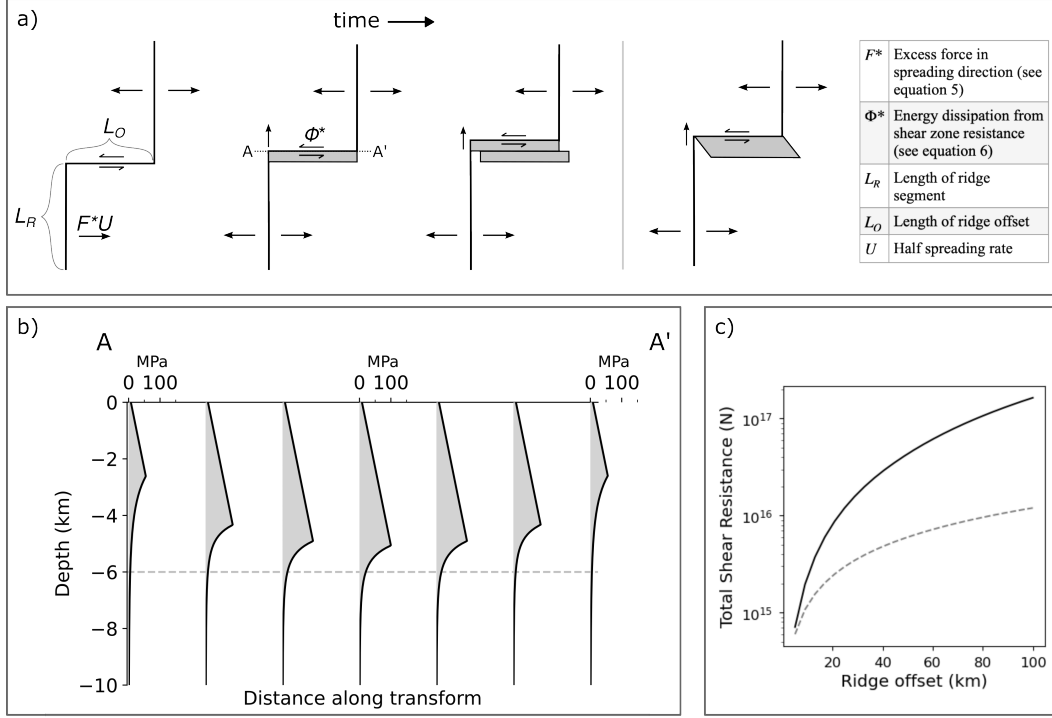


**Figure 3.** (a) Kinematics of a migrating ridge offset in plan view – as a ridge propagates, a finite zone is sheared to accommodate transform motion. Continuous shear deformation is shown on the right. Values and limits of integration in equations 5 and 6 are annotated and listed in the table. (b) Yield strength envelope versus depth using a modified halfspace cooling model for the profile AA'. Yield strength is integrated over depth and length of the offset to estimate total shear strength of a 2D offset zone. (c) Total shear strength in offset zone as offset length increases. Solid line is for a yield strength envelope model with coefficient of friction of 0.7. Dotted line is the total resistance using an average shear strength of 10 MPa.



$S$  is the vertically-integrated yield strength at a point along the offset and  $L_O$  is the length of the offset. Since both sides of equation 4 contain the spreading rate  $U$ , we can compare the forces instead of energy:

$$F^* \geq 2 \int_{L_O} S dL. \quad (7)$$

We will then refer to the transform resisting force rather than the transform energy dissipation. We emphasize that this yield strength is not the same as the strength of the mature transform fault which is known to be weak.

This model describes the propagation of one ridge segment – the implicit assumption is that the adjacent “failing” ridge has an excess force ( $F_{FR}^*$ ) of zero. For a ridge-offset-ridge system where either segment has an excess force in the spreading direction, both segments contribute to the instability of the offset, so the excess ridge forces will sum ( $F^* = F_{PR}^* + F_{FR}^*$ ). What then determines which segment propagates and which fails or which direction the ridge offset migrates? We posit that a greater total excess force along one ridge should cause a migration of the offset in the direction of the lower excess force ridge ( $F_{PR}^* > F_{FR}^*$ ). An implication of this is that propagation will continue in the same direction unless the state of loading along the ridge segments changes, but these dynamical problems are outside the scope of this study.

We use simple thermal models along with models of the yield strength of the cooling oceanic plate to calculate the transform resistive force from migration of the shear zone ( $\Phi_O^*/U$ ). This force depends on the age offset of the ridges. For example, the lithosphere on either side of a large offset transform is very strong because it is colder, so there is a great resistance that must be overcome.

### 3 Methods

#### 3.1 Yield strength envelope

To assess the strength of the lithosphere and the force required to migrate a ridge offset, we use a brittle failure criterion as defined by Byerlee’s law and a ductile flow criterion described by power law flow. Byerlee’s law describes the maximum shear stress that rock can support without brittle failure and has the form  $\tau_s = S_0 + \mu\sigma_n$  where  $\sigma_n$  is the normal stress,  $S_0$  is an inherent shear strength, and  $\mu$  is the coefficient of friction (Byerlee, 1978). Byerlee’s law assumes potential failure on all possible planes, so this stress is a lower bound. Byerlee (1978) found that  $\mu = 0.85, S_0 = 0$  at low pressure and  $\mu = 0.6, S_0 = 50$  MPa at higher pressures, independent of rock type. We will consider yield strength models with frictional coefficients as low as 0.3. Additional parameter values are given in Appendix A.

The power law flow model describes the maximum differential stress the lithosphere can support without ductile yielding. This value depends on strain rate, temperature (age), and experimentally determined parameters dependent on the composition of the medium (Goetze, 1978; Watts, 2001). We find that varying strain rate does not strongly affect the integrated strength, so we use a constant strain rate of  $1\text{e-}14 \text{ s}^{-1}$ . Full flow law details and parameter values are given in Appendix A.

The ductile yield strength depends strongly on temperature of the medium. Near a ridge axis where the crust is hot and newly formed, ductile strength is low and the ductile flow law describes the yield strength. As that material moves away from the ridge and cools, the ductile strength increases beyond the brittle strength, changing the failure regime (Figure 3(b)). There are many different models to describe the cooling of the oceanic lithosphere with age. Two simple 1-D models are the halfspace cooling model and plate cooling model which are basically identical for ages less than 50 Ma.



Simple thermal models don't account for variations in temperature along a spreading axis. They will work well for the middle of a ridge segment, but our areas of concern are ridge tips and discontinuities where there is variability in temperature in the ridge-parallel dimension. Modern ridge thermal models address the problem of ridge offsets (e.g. Behn et al., 2007; Grevenmeyer et al., 2021), but they can be computationally expensive and, because these studies focus on large transform faults, it's unclear that they apply to shorter offsets. Abercrombie and Ekstrom (2001) approximated transform fault thermal structure by averaging two halfspace thermal profiles on either side of a transform, and Behn et al. (2007) found this model produced thermal profiles similar to their 3-D finite element model. We consider this simple averaging of halfspace cooling models as our preferred cooling model.

Between brittle and ductile yield stress, the lesser value determines the overall yield strength envelope. For a given age or distance along an offset, we integrate the yield strength over the thickness of the lithosphere to estimate the strength as a function of age ( $S$  in equation 6).

### 3.2 Driving forces: estimating $F^*$

We model the driving force as the topographic ridge push force in the direction of spreading. We derive the ridge push force from the stress tensor field. The ridge push force acting from a point  $A$  to a point  $B$  is related to the difference in pressure at depth at the two points:

$$F_s = \int_{-L}^0 \Delta P(z) dz, \quad (8)$$

where  $L$  is the depth of compensation. From conservation of momentum, the horizontal forces at  $A$  and  $B$  must balance,  $F_{HA} = F_{HB}$ . If we have:

$$F_{HB} = \int_{-L}^0 P_B(z) dz, \quad (9)$$

then:

$$F_{HA} = \int_{-L}^0 P_A(z) + \tau(z) dz \quad (10)$$

$$\int_{-L}^0 \tau(z) dz = \int_{-L}^0 \Delta P(z) dz. \quad (11)$$

So the ridge push force from  $A$  to  $B$  is equivalent to the integrated deviatoric normal stress in the direction of  $AB$ .

We compute the stress field in the crust using the method of Luttrell and Sandwell (2012). Excess topography is treated as a vertical load acting on the crust. We then compute the isostatic balancing force on the Moho, which depends on the elastic thickness of the plate. These loading functions are convolved with the Greens function response for a point load, and the stresses are calculated from the displacement field. We use a Moho depth of 6 km, elastic thickness of 0 km (Airy compensation), and crustal density of  $2900 \text{ kg m}^{-3}$ .

As discussed above, ridge propagation is driven by the excess topography of the spreading ridge with respect to the normal topography needed to drive seafloor spreading. We assume this excess topography is near the ridge. In order to isolate this topography and calculate the excess driving force from a global topography grid we first need to remove large topographic variations related to continents, trenches and other major features that would dominate the stress computation. This was accomplished by masking all continents and oceanic crust older than 70 Myr. The remaining submarine topography is scaled by a factor of  $(\rho_c - \rho_w) / \rho_c$  to account for the load of the water column. The topography is then high pass filtered with a cosine taper from spherical harmonic

degrees 10 to 20 ( $\approx 3600$  km to 1900 km). The filtering removes the longest wavelength topographic signals such as the overall negative topography of the ocean basins, but we note that these harmonic degrees are somewhat arbitrary (see discussion).

After determining the stress field due to topography, we determine the normal tractions acting along a vertical surface that coincides with the ridge segment (surface normal  $\sim$  parallel to spreading direction). We integrate these tractions along the ridge segment to estimate the loading force  $F^*$  (equation 5).

### 3.3 Digitized ridge segments and offsets

To apply equations 5 and 6 to real ridge-offset-ridge systems, we approximate the mid-ocean ridge system as a series of spreading segments and lateral offsets. The off-axis SSPs were described and digitized by Harper et al. (2021). For the present day SSPs in that set (i.e., they can be traced continuously to the ridge axis), we digitize the adjacent ridge segments and the offset. All of these features are approximated as simple line segments.

For most of these features, the spreading center has an axial valley morphology and appears as a distinct local low in the VGG. The morphology in the greater offset zone varies in complexity, but offsets are typically associated with slight VGG lows. The offset is digitized to approximately connect the tips of the adjacent ridge segments. Of the two ridge segments per feature group, one is called the propagating ridge and one the failing ridge based on the propagation direction determined from the off-axis morphology of the SSP. Additional details and an example of a digitized feature group are given in Appendix B. In many cases, the rate of propagation may be low enough or the deformation patterns too complex to confidently determine the present direction of propagation (see Discussion).

In all, we digitize 55 ridge-offset-ridge features for model evaluation. We additionally digitize 69 ridge-transform fault-ridge features in a similar manner. We restrict the set of transform faults to the same ridge systems where we identify SSPs – i.e., the northern and southern Mid-Atlantic Ridge, the central and southeast Indian Ridge, and the Nazca-Antarctica Ridge. For each digitized ridge-offset-ridge feature, we estimate an offset shear resistance based on a range of yield strength models (friction coefficient of 0.3 to 0.7). For the ridge segments, we estimate a loading force using the method described above. The success of the model is evaluated by two tests. The first tests the condition for instability described by equation 7. We add the loading forces of the two ridge segments and compare the sum to the offset shear resistance. If the condition for instability is met, then this test passes. The second tests whether the model predicts the right (observed) direction of propagation. The loading force of the propagating ridge segment ( $F_{PR}^*$ ) is compared to the loading force of the failing ridge segment ( $F_{FR}^*$ ), and if  $F_{PR}^* > F_{FR}^*$ , then this test passes.

## 4 Results

### 4.1 Major propagating ridges

We first test this model on major propagating ridges in two regions: the Cocos-Nazca spreading center and the southeast Indian Ridge (Figure 4a-b). We selected these systems because the propagation direction is unambiguous and has remained uniform over time. These tests are, in a loose sense, to validate the model approach and parameter selection – i.e., if the conditions for ridge propagation are not met at these obvious cases, then some part of the model is flawed.

The section of the Cocos-Nazca spreading center between the Galapagos hotspot and the Galapagos Triple Junction contains one of the earliest observed propagating ridges

(Hey & Vogt, 1977) (Figure 4a). The primary feature in a suite of westward-propagating segments is a  $\sim 500$  km long segment bounded to the east by the Galapagos Transform Fault. To the west, the segment is truncated by a  $\sim 40$  km offset which is followed by a  $\sim 100$  km long failing ridge. The present half spreading rate is 30 mm/yr, and the ridge propagates westward 50 mm/yr relative to the plate boundary (Hey et al., 1980). In the VGG maps, the inner pseudofault/sheared zone appear as a low, trending WNW-ESE, but the outer pseudofault does not have a strong signal. The Galapagos propagating ridge has been modeled with a fracture mechanics approach by Morgan and Parmentier (1985) who developed the energy balance we begin with in this study.

The suite of propagating ridges in the SEIR are not as well-studied as the Galapagos case, but the signature in the VGG maps is striking (Figure 4b). The series of westward propagating segments lies to the east of the Australian-Antarctic discordance, an anomalously deep section of the ridge (Palmer et al., 1993). The ridge segments are axial highs, and the half spreading rate is  $\sim 34$  mm/yr (Seton et al., 2020). In the VGG maps, the outer pseudofaults appear as continuous lows trending NE-SW, and the inner pseudofaults/sheared zones appear as linear discontinuous highs (ridges) trending NW-SE. Morgan and Sandwell (1994) identified these propagators using Geosat-derived gravity data and estimated propagation rates of 40-49 mm/yr based on the geometry of the outer pseudofaults and NUVEL-1 spreading rates (DeMets et al., 1990). Another study of propagating ridges along the SEIR, West et al. (1999), includes the western-most of these features (SEIR\_03).

Model results for each of these ridge-offset-ridge systems are shown in Figure 4c-d. The first test checks that the total loading force (the sum of the propagating and failing ridge forces) exceeds the resistance associated with the migration of the shear zone (calculated from equation 6). The estimated shear resistance depends strongly on the choice of coefficient of friction, so these values are shown as a gray bar representing the range of 0.3 to 0.7. In all 4 cases, the total loading force exceeds the shear resistance of the ridge offset for even the greatest friction coefficients, predicting that these segments are unstable and will propagate. The magnitude of these forces is, to first order, related to the length of the features. The longer ridge segments have greater loading forces,  $F^*$ , and the shorter segments have the lowest loading forces (e.g. Galapagos FR, SEIR\_03). Shear resistance,  $\Phi_O^*/U$ , is also related to the length of the offset. Among these features, the offset lengths don't vary greatly, so neither do the estimates shear resistance.

The second test checks that our model correctly predicts the observed propagation direction. For each of the features shown in Figure 4a-b, 4d shows the estimated force along the adjacent propagating ridge (calculated from equation 5) compared to the estimated force along the adjacent failing/retreating ridge. In order for each ridge to propagate in the observed direction, we expect the force along the propagating segment to exceed the force along the retreating segment. We find this is the case at three of the four offsets considered (Galapagos, SEIR\_03, SEIR\_02), while at the fourth (SEIR\_01) the forces along the propagating and retreating segments are about equal. As mentioned in the first test, the ridge segment length is the greatest influencing factor on  $F_{PR}^*$  and  $F_{FR}^*$  here.

We have applied the model and tests to four cases of major propagating ridges, and we see the approach correctly predicts the migration of the ridge offsets for these cases. The test for propagation direction succeeds in three of the four cases. Next, we apply our model method to a larger catalog of ridge-offset-ridge features, both those that are observed to propagate and transform faults.

## 4.2 Transform faults

An important test of our model framework is that, in addition to predicting propagation, it should also predict stability at transform faults. Figure 5 shows the total load-

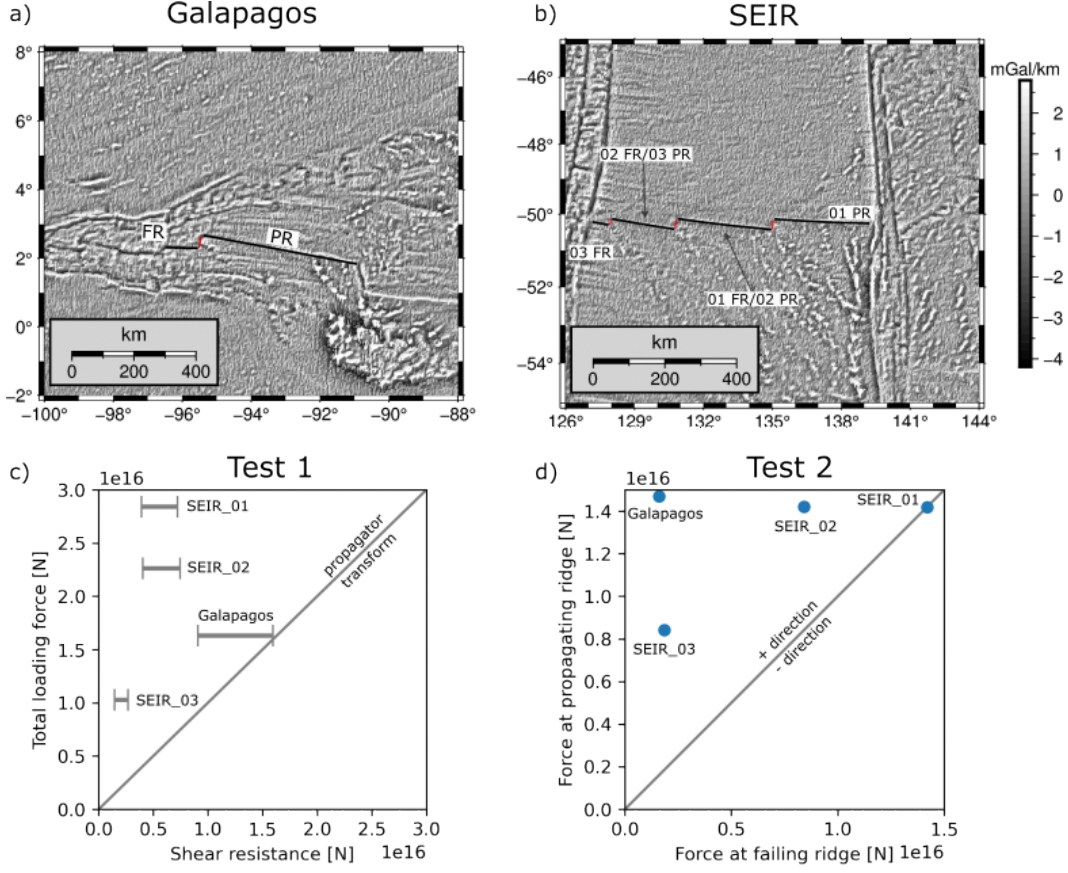


**Figure 4.** Vertical gravity gradient map view of (a) Galapagos propagating ridge and (b) southeast Indian propagating ridges. Individual segments (black lines) and offsets (red lines) are labeled. PR = propagating ridge, FR = failing ridge. (c) The total loading force on the ridge segments ( $F_{PR}^* + F_{FR}^*$ ) vs the estimated shear resistance of the migrating offset. Area above the solid line (1:1) indicates the loading force exceeds the resistance and the offset is unstable. A range of strength models is shown, with friction coefficients from 0.3 (weakest) to 0.7 (strongest). (d) Loading forces on the failing and propagating ridges for the systems shown in (a,b). Solid gray line is 1:1.

ing force versus shear resistance for a set of 69 stable ridge-transform-ridge features, calculated using the same approach as Figure 4c. Across this set of features, there is a much wider range of shear resistance and total loading force values (note the logarithmic scales). For each feature, even the weakest shear resistance estimates exceed the loading force, typically by an order of magnitude or more. This is consistent with the observed stability of the features. The results for transform faults, especially when compared to the propagating ridge results, give us confidence that the model framework can distinguish between transform faults and propagating ridges/migrating offsets.

### 4.3 Seesaw propagators

Now we apply the model to the set of present day seesaw propagators (SSPs). The set of 55 SSPs comprises 34 features from the north and south Mid-Atlantic Ridge, 17 from the northern and southeast Indian ridge, and 4 from the Nacza-Antarctic ridge. All of these ridge segments have axial valley morphologies. For this set of features, the half spreading rates range from 11 mm/yr to 37 mm/yr.

The results of the model tests are shown in Figure 6. Using the same driving force model as above, the estimated resisting force is too great to allow offset migration for many of the features (35/55) for even the weakest models of strength.

For 41/55 SSPs, the observed propagation direction is predicted by the model ( $F_{PR}^* > F_{FR}^*$ ) (Figure 6b). Among the features that fail either of these tests, there are no exclusive underlying similarities (e.g., they aren't clustered spatially, no spreading-rate dependence). Among the features where the total loading force exceeds the shear resisting force, 18/20 of the observed propagation directions are predicted. There are 8/55 features with net negative loading forces. A negative loading force indicates the stress due to topography resists plate motion.

## 5 Discussion

In this study, we've built on the model framework proposed by Morgan and Parmentier (1985) to examine the stability of spreading ridge offsets and the relation to offset length and strength of the lithosphere. We posited that the forces driving ridge propagation must at least exceed the shear resistance of the lithosphere in the migrating shear zone region. We examined the success of this model framework with two tests applied to real ridge-offset-ridge features to determine whether the model 1) predicts the observed stability or propagation of a feature and 2) predicts the observed direction of propagation of a feature.

This model of ridge-offset stability succeeds for four cases of major ridge propagation (offset migration is possible). The model succeeds for all 69 cases of transform faults (stability is predicted). For slow-spreading seesaw propagators, the model only succeeds (offset migration is possible) in 20/55 cases using a yield strength envelope with a frictional coefficient of 0.3. The observed propagation direction is predicted by the model for 41/55 cases.

The model tests fail if the total loading force does not exceed the offset shear resistance or the failing ridge loading force exceeds the propagating ridge loading force. For the set of SSPs, there are only 20/55 cases where the first test passes, even using the weakest models of lithospheric strength. Considering a coefficient of friction as low as 0.1 does improve the results for SSPs (35/55 pass), but a strength model this weak would allow offset migration at one transform fault.

For SSPs, there are 14/55 cases where the wrong propagation direction is predicted. We consider that for such low rates of propagation or complex deformation patterns near the ridge axis, it's difficult to confidently label which ridge segment is presently prop-

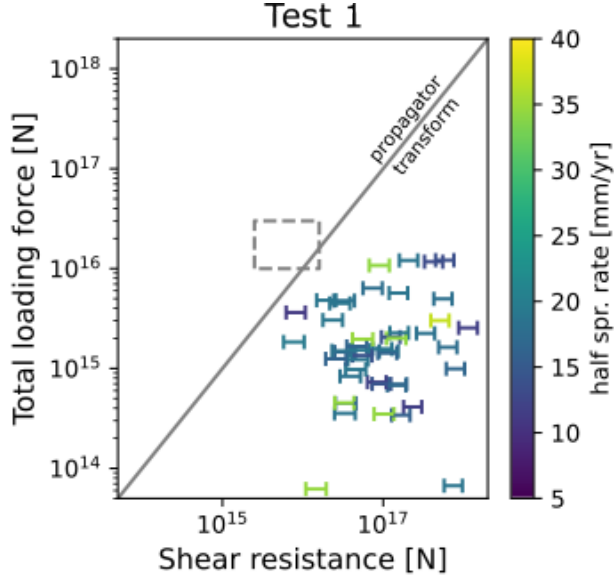


**Figure 5.** Results for stable transform fault offsets: total loading force on adjacent ridge segments vs. the estimated shear resistance of a migrating offset. Area below the solid gray line (1:1) indicates the shear strength exceeds the available loading force. Note the logarithmic scales. A range of strength models is shown with friction coefficients from 0.3 (weakest) to 0.7 (strongest). Points are shaded by half spreading rate (Seton et al., 2020). Dash-outlined box shows the range of values in Figure 4c.

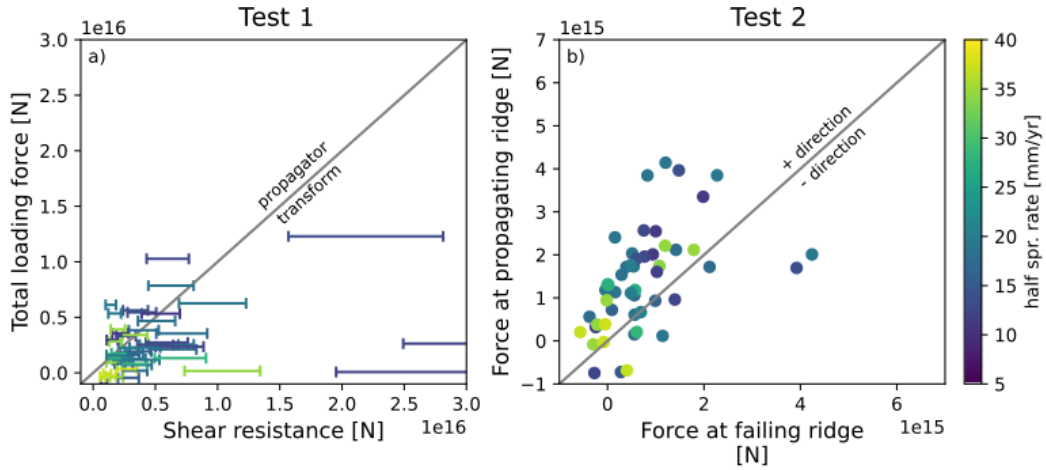


**Figure 6.** (a) The total loading force on the ridge segments ( $F_{PR}^* + F_{FR}^*$ ) vs the estimated shear resistance of the migrating offset for the set of seesaw propagators (SSPs). Area above the solid line (1:1) indicates the loading force exceeds the resistance and the offset is unstable. A range of strength models is shown, with friction coefficients from 0.3 (weakest) to 0.7 (strongest). (b) Loading forces on the failing and propagating ridges for the set of SSPs. Solid gray line is 1:1. Points are shaded by half spreading rate (Seton et al., 2020).



agating. We select 24 of the 55 SSPs for which we can confidently identify the present propagation direction, and find 20/24 are correctly predicted by the model – this is not much of an improvement, and we don’t believe this explains much of the model’s inaccuracy. There are many simplifying assumptions in the calculations and model framework that may contribute to the cases of failure, and we will examine those here.

## 5.1 Shear resistance exceeds loading force

For propagating ridges, the first model test fails when the total propagation force does not exceed the shear resistance associated with migrating the offset (equation 7 does not hold). The failure of the model in this way could be a result of overestimating the real strength of the lithosphere, or underestimating the real driving forces of propagation.

First, we will consider that the yield strength envelope model is overestimating the strength of the lithosphere. In estimating the total offset resistance, the most important component is the length of the offset. Each offset has a measured spreading rate which is inversely proportional to the total strength (but is proportional to the dissipation rate). The other yield strength parameters are free. For a given length offset, the total offset dissipation is most sensitive to the chosen friction coefficients. However, the friction coefficients we have considered (0.3) are very low. Even with a friction coefficient of 0.1, 20/55 of the seesaw propagators fail this test.

The other major influence on yield strength is the temperature of the medium. At the ridge-offset intersection, 3-D variations in thermal structure are significant. Simple 2-D thermal models can’t be applied without some modification (the total strength will be far too high). We use the simple approach of averaging two temperature profiles to overcome this problem (Abercrombie & Ekstrom, 2001). There are some differences in the resulting isotherms compared to a more sophisticated model – e.g., Behn et al. (2007) predict isotherms are deepest at ridge-offset intersections rather than the offset midpoint. However, the total strength would not be affected by this.

In addition to a possible overestimate of lithospheric strength, our estimate of ridge loading force may also be biased. In describing the methods for calculating  $F^*$ , we mentioned the masking and filtering steps we apply to the global topography. One of the goals of this processing is to approximately separate the long wavelength force driving plate motion,  $F$ , from the short wavelength force,  $F^*$ , from excess topography. Using the filter approach, we must decide on appropriate spherical harmonic degrees for the cosine taper, so there is ambiguity in the absolute magnitude of the ridge push force. We note that as longer wavelengths are removed from the input topography model, the estimated force decreases, and fewer example features will have sufficient loading force to overcome the offset shear resistance.

In addition, there are some constraints in the stress model that are worth exploring. We presented model results for uniform crustal thickness of 6 km. Using a slightly thicker crust of 8 km, the first order effect will be an increase in loading force since the limits of integration in equation 8 are increased by 2 km. Increasing the crustal thickness to 8 km globally, the test results improve to 30/55 cases passing. However, the thicker crust changes the internal stress field in ways that are not obvious, and the predictions of propagation direction suffer.

### 5.1.1 Model framework

Beyond necessary simplifications in the calculations of force and resistance, there are physical processes our model framework doesn’t include. One possibility is that the mechanism of deformation is not accurately described by our model. Perhaps a two-stage accretion model (Grevemeyer et al., 2021) or the local off-transform deformation of the



crust (Zhang et al., 2022) may create instabilities and initiate the onset of propagation episodes. We also note the lack of excess resisting forces along the ridge axis in our model – however, the exclusion of these doesn’t interfere with the criterion that the driving forces must at least exceed offset shear resistance.

Finally, loading forces that are not expressed in the topography may influence the stability of offsets or the direction of ridge propagation. Our model has assumed all of the loading force is due to excess topography. There are possibly non-isostatic regional forces such as along-ridge asthenosphere flow driving ridge offset instability (e.g. West et al., 1999). Segment-scale effects such as dynamic upwelling of magma sources may provide additional propagation forces (e.g. Zheng et al., 2019). Such localized effects are likely important for seesaw propagators, where propagation direction is not consistent for adjacent features and changes over time.

## 5.2 Direction of propagation

The other type of model failure is when the driving force along the observed failing ridge exceeds the driving force along the propagating ridge  $F_{FR}^* > F_{PR}^*$ . Why might the model fail in these cases? The discussion of the biases in estimating loading force applies to this problem as well. When the input topography is filtered to shorter wavelengths, the results change in non-obvious ways. Using a cosine taper filter from spherical harmonic degrees 20 to 30 ( $\sim 1900$ – $1290$  km), the results for this test are slightly worse (38/55 pass). As mentioned in the previous section, when more long wavelength topography is removed, the total loading force is too small.

The same factors regarding the ridge loading model framework mentioned in the previous section are also important here. It’s possible we are missing non-isostatic driving forces contributing to loading on either ridge segment. It’s important to note that for SSPs, the observed direction of propagation is not consistent spatially – i.e., adjacent propagators do not necessarily propagate in the same direction. For this reason, we believe local effects are more likely than missing regional mechanisms.

Finally, our model attempts to isolate ridge-offset-ridge features from the greater series of spreading ridges and offsets that comprise the whole mid-ocean ridge system. For example, how does one propagating ridge/migrating offset affect the adjacent ridge offsets – are propagation forces that aren’t dissipated within that feature added to the propagation force of another segment? The complex inter-relationships of such a system are beyond the specific scope of this model.

## 5.3 Comparisons to other models

As previously stated, our model is based on an energy balance presented by Morgan and Parmentier (1985), and we will clarify some key differences between our models. One major difference is in our treatment of the forces resisting propagation where we suggest the limiting factor is resistance associated with migrating the ridge offset. In contrast, Morgan and Parmentier (1985) models the limiting resistive process as dynamic viscous forces in an axial magma chamber – we don’t model any viscous processes on the ridge axis. Calculating a viscous resisting force requires an estimate of propagation rate which, for many of the features in this study, is very low.

West et al. (1999) applied the Morgan and Parmentier (1985) model framework to five propagating ridges of the southeast Indian Ridge. Four of these features lie to the west of the Australian-Antarctic discordance (AAD) and presently propagate eastward; the other (the same feature as SEIR\_03 of this study) lies to the east of the AAD and propagates westward. Their application of the model predicts the incorrect sense of propagation for all features, so they require an additional regional force, along-axis asthenospheric flow, to drive propagation towards the AAD. This study includes four of the five

features from West et al. (1999), and for each of those, the condition for instability is met for low coefficients of friction and the correct direction of propagation is predicted.

Complex propagation patterns are likely a result of variations in mantle melting at individual ridge segments, and this is treated more explicitly in magmatic models such as Tucholke et al. (1997); Dannowski et al. (2018); Zheng et al. (2019) among others. For example, increased melt supply at a segment will increase the amount of plate motion accommodated by magmatic emplacement and decrease ridge-normal strain, while segments with decreased melt supply will undergo increased tectonic strain (e.g. Wang et al., 2015). Varying tectonic strain rates at adjacent segments may result in ridge propagation, but in some cases the along-ridge migration of a magmatic body may be what drives ridge propagation (Martinez et al., 2020). Such models are not necessarily mutually exclusive to our approach since our driving forces, calculated from topography, are likely magmatic in origin. A possible implication of magmatic models is that the migration of short offsets (and stability of larger offsets) is related to the continuity of mantle upwelling regimes (Martinez & Hey, 2022). This is quite different from our yield strength hypothesis, but not mutually exclusive, since migration of a shear zone is still necessary. However, in our model, we do not account for differing strength profiles that may be the result of complex mantle melting patterns (Martinez & Hey, 2022).

#### 5.4 Model implications

Estimates of ridge loading forces may be biased and the modeling of deformation may be too simplistic to explain all cases of ridge propagation, but conceptually this model attempts to describe a ridge segment system that wants to constantly evolve but is held together or buttressed by strong lithosphere at long offsets. When excess driving forces are great enough, this configuration is degraded. This is why large-scale regional anomalies, even if the offsets are of great length, can propagate. This also explains why those large propagators are mostly unidirectional as the driving force is not likely to rapidly reverse. Short offsets, where the energy requirement is not so great, may migrate in response to smaller changes along ridge segments – changes that reverse relatively quickly, resulting in “seesaw” propagation and general offset instability. The question remains – what are the causes of seesaw propagation? There are many non-exclusive potential mechanisms, but they are most likely related to complex patterns of small-scale mantle melting and convection (Dannowski et al., 2018; Zheng et al., 2019; Martinez & Hey, 2022). Our model is agnostic to the origin of these forces, but assumes they are expressed topographically. Similarly, the lengthening or shortening of an offset and the transition from unstable to stable offset, or vice versa (e.g. Matthews et al., 2011), is not explained by our model.

We have mentioned that our model of shear zone deformation may be too simplistic to explain all cases of ridge propagation. Using the basic yield strength envelope approach, we have made some qualitative observations of offset zone lithospheric strength that we believe may be related to ridge offset stability. Depending on the choice in crustal rheology, a weak zone may develop in the lower crust where ductile crust overlies a rigid mantle. This modeled weak zone resembles the decoupling layer suggested by Chen and Morgan (1990), and it is possible that the presence of a lower decoupling region in the offset zone aids offset migration by reducing the shear strength of the lithosphere.

Plate coupling introduces additional complexities to shear zone deformation and the physics of our model. If plate coupling at an offset is too low, the energy from excess spreading force will not all be dissipated by shear deformation. At weakly-coupled transform faults, this would effectively reduce the total loading force of the ridges. In our model, we are establishing a threshold on how much energy is required to migrate an offset, and this should be independent of the plate coupling. The influence of plate coupling, especially as the quantity varies with offset length or how it might relate to

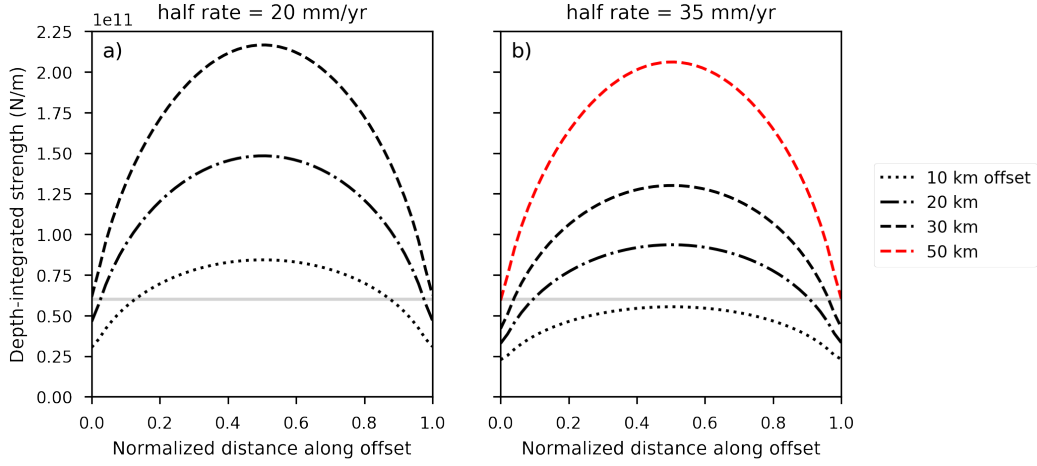


**Figure 7.** Depth-integrated shear strength vs. normalized distance along an offset for growing offset length. (a) friction coefficient of 0.7, crustal thickness of 6 km, half spreading rate of 20 mm/yr; (b) friction coefficient of 0.7, crustal thickness of 6 km, half spreading rate of 35 mm/yr. In both figures, the solid line is the strength of a theoretical transform fault using an estimated 10 MPa shear strength (integrated over a 6 km crust).

the yield strength envelope, is surely important to the problem of ridge propagation, but we have not addressed those complexities here.

#### 5.4.1 Minimizing resistance

Recall the classic argument that the configuration of ridges and transform faults seeks to minimize the resistance to plate motion (Lachenbruch & Thompson, 1972). Assume, for any ridge offset, there is a transform fault with a given average shear strength of 10 MPa. For short offsets, it may be that the strength of the lithosphere (computed from the YSE) is weaker than a transform fault, so the transform fault is not the path of least resistance. By seeking to minimize the resistance to spreading motion, off-transform deformation and ridge propagation may result from young, weak lithosphere.

Figure 7 shows such a comparison of yield strength at an offset to an average strength of 10 MPa typical of oceanic transform faults (Morgan & Parmentier, 1984). For shorter offsets, the relatively weak lithosphere may accommodate shear strain with less resistance than a pre-existing transform fault, and deformation proceeds into an overlap zone. For larger offsets, the lithosphere is stronger than the transform fault, so deformation is confined to this weakly-resistant zone. There will be variability in this offset length threshold due to real thermal complexities, spreading rate, and crustal thickness, but this simple argument avoids assumptions about the ridge loading force.

## 6 Conclusions

We began this study with observations of seesaw propagating ridges at slow- and intermediate-spreading sites. For this set of SSPs, the maximum ridge offset length is about 30 km – larger offsets are transform faults, and ridge propagation is rarely observed. We hypothesized that the strength of the lithosphere at a ridge offset limits whether a ridge can propagate and that this could explain the threshold offset length between propagating ridges and transform faults. Adapting a framework developed by earlier work-

ers, we tested this hypothesis on observed transform faults and propagating ridges/migrating offsets. We found that major propagating ridges and transform faults support our framework. For a set of seesaw propagators, the model framework does not work strictly, but it's clear that the features are a population distinct from stable transform faults. It stands that the weak lithosphere at small offsets is essential to produce ridge propagation and, conversely, that strong lithosphere at transform faults contributes to their stability.

## Appendix A Yield strength envelope parameters

### A1 Brittle strength parameters

To compute the brittle strength of the lithosphere, we use Byerlee's law which has the form:

$$\tau_S = S_0 + \mu\sigma_n, \quad (\text{A1})$$

where  $S_0$  is the cohesion,  $\mu$  is the coefficient of friction, and  $\sigma_n$  is the normal stress. Although Byerlee (1978) suggested a piecewise function for low and high normal stress, the models in this study use a single coefficient of friction (or a range of coefficients for different models) and zero cohesion. The normal stress is a combination of water column overburden, rock overburden, and pore fluid pressure. We give the top 6 km of the lithosphere (the crust layer) a density of  $\rho_c = 2900 \text{ kg m}^{-3}$  and the deeper lithosphere a density of  $\rho_m = 3300 \text{ kg m}^{-3}$ . In the top 6 km, we include the influence of pore fluids as a ratio of pore fluid pressure to lithostatic pressure (Brace & Kohlstedt, 1980) which has the effect of lowering the brittle yield strength.

### A2 Ductile flow law and parameters

The ductile strength is computed using a power law flow model (Goetze, 1978) which has the form:

$$\tau_S = \left( \frac{\dot{\epsilon}}{A} \right)^{1/n} \exp \left( \frac{Q}{nRT} \right) \quad (\text{A2})$$

$T$  is temperature,  $R$  is the ideal gas constant. The material constant  $A$ , activation energy  $Q$ , and stress exponent  $n$  are laboratory-derived quantities dependent on mineral composition. We use parameters for wet olivine in the top 6 km ( $n = 3$ ,  $A = 1.9\text{e-}15 \text{ Pa}^{-n} \text{ s}^{-1}$ ,  $Q = 4.2\text{e}5 \text{ J mol}^{-1}$ ) (Karato et al., 1986), and dry olivine in the lower lithosphere ( $n = 3.5$ ,  $A = 2.4\text{e-}16 \text{ Pa}^{-n} \text{ s}^{-1}$ ,  $Q = 5.4\text{e}5 \text{ J mol}^{-1}$ ) (Karato et al., 1986). Strain rate  $\dot{\epsilon}$  is set to  $1\text{e-}14 \text{ s}^{-1}$ .

## Appendix B Example digitized ridge segments

Because the VGG includes the gravitational effects of both bathymetry and the Moho, it is a better independent resource for identifying the ridge axis than bathymetry alone. However, when the ridge axis is not obvious in the VGG, we use depth data from SRTM15+V2 (Tozer et al., 2019) to help identify the extent of the ridge. Figure B1 shows an example of digitized ridge segments and ridge offset. While high-resolution bathymetry shows greater short-wavelength detail than the vertical gravity gradient (VGG), the ridge axis is more prominent in the VGG. Subtle ridge discontinuities such as devals are ignored in our digitizations, and they are suppressed in the VGG due to a lack of Moho compensation. Ridge segments are terminated at offsets or, in some cases, changes in trend of ridge axis.

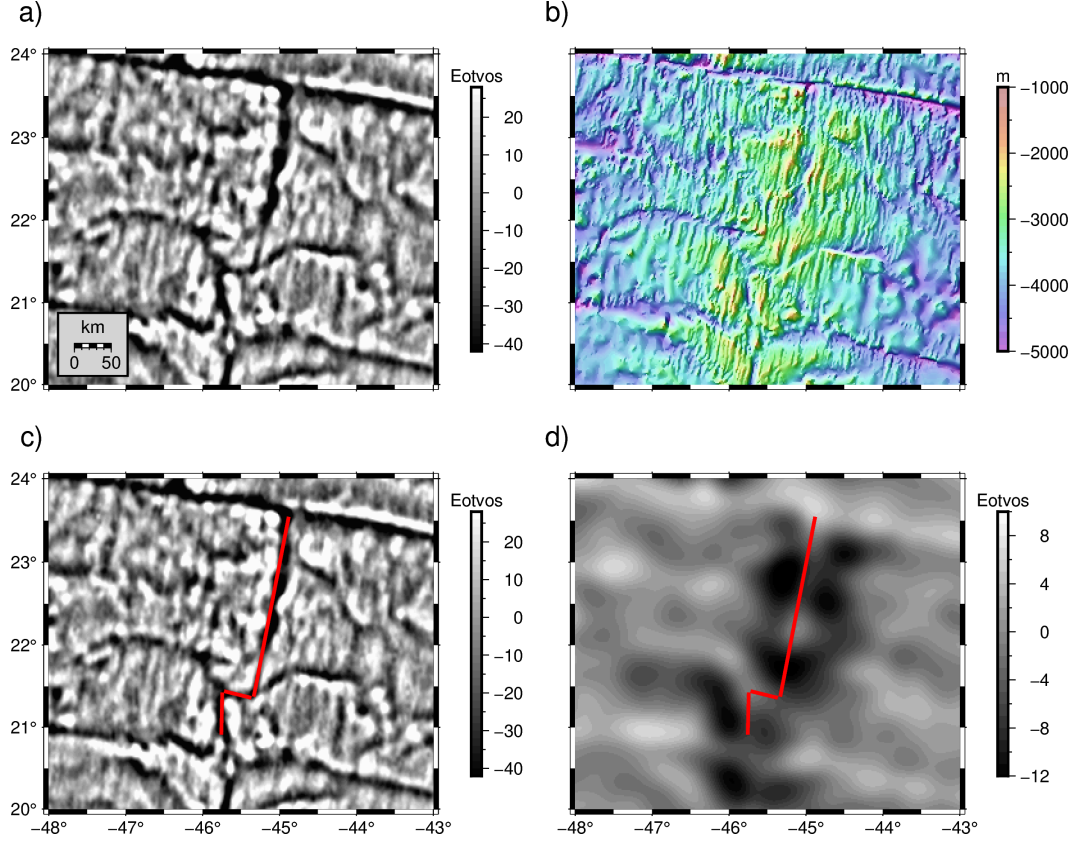


**Figure B1.** An example in the North Atlantic. a) Satellite-derived vertical gravity gradient (VGG). b) Bathymetry at 15 arc second resolution (Tozer et al., 2019). c) The VGG with digitized ridge segments and migrating offset shown in red. d) The VGG signal from the Moho, computed from bathymetry, a mean crustal thickness of 6 km, and an elastic thickness of 3.2 km that minimizes rms error near the ridge axis; digitized features from (c) are overlain.

## Open Research Section

### Data Availability Statement

Predicted depth data used in computations are attributed to Tozer and Sandwell (2019), as are vertical gravity gradient data used to digitize mid-ocean ridge features. Digitized ridge segments and offsets are given in Harper et al. (2023). Crustal age and spreading rate data are attributed to Seton et al. (2020). PyGMT (Uieda et al., 2022) and the Generic Mapping Tools (GMT) (Wessel et al., 2019) were extensively used in data processing. Maps and figures were made with PyGMT (Uieda et al., 2022) and Matplotlib (Hunter, 2007).

### Acknowledgments

We thank Ross Parnell-Turner, Dave May, and Jeff Gee for their suggestions and comments on an earlier version of the manuscript. We thank the associate editor and two anonymous reviewers for their constructive feedback that greatly improved the quality of this manuscript. This work was supported by the NASA SWOT program (80NSSC20K1138) and the Office of Naval Research (N00014-17-1-2866). Hugh Harper was supported by a NASA FINNEST fellowship (80NSSC20K1616).

### References

- Abercrombie, R. E., & Ekstrom, G. (2001). Earthquake slip on oceanic transform faults. *Nature*, *410*.
- Behn, M. D., Boettcher, M. S., & Hirth, G. (2007). Thermal structure of oceanic transform faults. *Geology*, *35*, 307-310. doi: 10.1130/G23112A.1
- Behn, M. D., Lin, J., & Zuber, M. T. (2002). Evidence for weak oceanic transform faults. *Geophysical Research Letters*, *29*, 1-4. doi: 10.1029/2002GL015612
- Boettcher, M. S., & Jordan, T. H. (2004). Earthquake scaling relations for mid-ocean ridge transform faults. *Journal of Geophysical Research: Solid Earth*, *109*, 1-21. doi: 10.1029/2004JB003110
- Brace, W. F., & Kohlstedt, D. L. (1980). Limits on lithospheric stress imposed by laboratory experiments. *Journal of Geophysical Research*, *85*, 6248-6252. doi: 10.1029/jb085ib11p06248
- Brozena, J. M., & White, R. S. (1990). Ridge jumps and propagations in the south atlantic ocean. *Nature*, *348*, 149-152. doi: 10.1038/348149a0
- Byerlee, J. (1978). Friction of rocks. In *Rock friction and earthquake prediction* (pp. 615-626). Springer.
- Carbotte, S. M., Smith, D. K., Cannat, M., & Klein, E. M. (2016). Tectonic and magmatic segmentation of the global ocean ridge system: A synthesis of observations. *Geological Society Special Publication*, *420*, 249-295. doi: 10.1144/SP420.5
- Chen, Y. J., & Morgan, W. J. (1990). Rift valley/no rift valley transition at mid-ocean ridges. *Journal of Geophysical Research*, *95*, 17571-17581.
- Dannowski, A., Morgan, J., Grevemeyer, I., & Ranero, C. (2018). Enhanced mantle upwelling/melting caused segment propagation, oceanic core complex die off, and the death of a transform fault: the mid-atlantic ridge at 21.5n. *Journal of Geophysical Research: Solid Earth*, *123*.
- DeMets, C., Gordon, R. G., Argus, D., & Stein, S. (1990). Current plate motions. *Geophysical journal international*, *101*(2), 425-478.
- Goetze, C. (1978). The mechanisms of creep in olivine. *Philosophical Transactions of the Royal Society of London. Series A, Mathematical and Physical Sciences*, *288*(1350), 99-119.
- Grevemeyer, I., Rüpke, L. H., Morgan, J. P., Iyer, K., & Devey, C. W. (2021). Extensional tectonics and two-stage crustal accretion at oceanic transform



- faults. *Nature*, 591, 402-407. Retrieved from <http://dx.doi.org/10.1038/s41586-021-03278-9> doi: 10.1038/s41586-021-03278-9
- Grindlay, N. R., & Fox, P. J. (1993). Lithospheric stresses associated with non-transform offsets of the mid-atlantic ridge: implications from a finite element analysis. *Tectonics*, 12, 982-1003.
- Grindlay, N. R., Fox, P. J., & MacDonald, K. C. (1991). Second-order ridge axis discontinuities in the south atlantic: Morphology, structure, and evolution. *Marine Geophysical Researches*, 13, 21-49. (Probably the key paper to cite.) doi: 10.1007/BF02428194
- Harper, H., Sandwell, D., & Luttrell, K. (2023, March). *Digitizations of seesaw propagating ridges*. Zenodo. Retrieved from <https://doi.org/10.5281/zenodo.7719237> doi: 10.5281/zenodo.7719237
- Harper, H., Tozer, B., Sandwell, D. T., & Hey, R. N. (2021). Marine vertical gravity gradients reveal the global distribution and tectonic significance of “seesaw” ridge propagation. *Journal of Geophysical Research: Solid Earth*, 1-16. doi: 10.1029/2020jb020017
- Hey, R. (1977). A new class of “pseudofaults” and their bearing on plate tectonics: A propagating rift model. *Earth and Planetary Science Letters*, 37, 321-325. doi: 10.1016/0012-821X(77)90177-7
- Hey, R. (2001). Propagating rifts and microplates. *Encyclopedia of Ocean Sciences*, 597-605. doi: 10.1016/B978-012374473-9.00095-3
- Hey, R., Duennbier, F. K., & Morgan, W. J. (1980). Propagating rifts on midocean ridges. *Journal of Geophysical Research*, 85, 3647-3658. doi: 10.1029/JB085iB07p03647
- Hey, R., Martinez, F., Höskuldsson, Á., & Benediktsdóttir, Á. (2010). Propagating rift model for the v-shaped ridges south of iceland. *Geochemistry, Geophysics, Geosystems*, 11(3).
- Hey, R., & Vogt, P. (1977). Spreading center jumps and sub-axial asthenosphere flow near the galapagos hotspot. *Tectonophysics*, 37, 41-52. doi: 10.1016/0040-1951(77)90038-5
- Hunter, J. D. (2007). Matplotlib: A 2d graphics environment. *Computing in Science & Engineering*, 9(3), 90-95. doi: 10.1109/MCSE.2007.55
- Karato, S.-I., Paterson, M. S., & Fitzgerald, J. D. (1986). Rheology of synthetic olivine aggregates: influence of grain size and water. *Journal of Geophysical Research*, 91, 8151-8176.
- Kleinrock, M. C., Tucholke, B. E., Lin, J., & Tivey, M. A. (1997). Fast rift propagation at a slow-spreading ridge. *Geology*, 25, 639-642. doi: 10.1130/0091-7613(1997)025(0639:FRPAAS)2.3.CO;2
- Lachenbruch, A. H., & Thompson, G. A. (1972). Oceanic ridges and transform faults: their intersection angles and resistance to plate motion. *Earth and Planetary Science Letters*, 18.
- Luttrell, K., & Sandwell, D. (2012). Constraints on 3-d stress in the crust from support of mid-ocean ridge topography. *Journal of Geophysical Research: Solid Earth*, 117, 1-19. doi: 10.1029/2011JB008765
- Martinez, F., & Hey, R. (2022, 2). Mantle melting, lithospheric strength and transform fault stability: Insights from the north atlantic. *Earth and Planetary Science Letters*, 579. doi: 10.1016/j.epsl.2021.117351
- Martinez, F., Hey, R., & Ármann Höskuldsson. (2020, 7). Reykjanes ridge evolution: Effects of plate kinematics, small-scale upper mantle convection and a regional mantle gradient. *Earth-Science Reviews*, 206. doi: 10.1016/j.earscirev.2019.102956
- Matthews, K. J., Miller, R. D., Wessel, P., & Whittaker, J. M. (2011). The tectonic fabric of the ocean basins. *Journal of Geophysical Research: Solid Earth*, 116, 1-28. doi: 10.1029/2011JB008413
- Morgan, J. P., & Parmentier, E. (1984). Lithospheric stress near a ridge-transform



- intersection. *Geophysical Research Letters*, 11.
- Morgan, J. P., & Parmentier, E. (1985). Causes and rate limiting mechanisms of ridge propagation: A fracture mechanics model. *Journal of Geophysical Research*, 90, 8603-8612.
- Morgan, J. P., & Sandwell, D. T. (1994). Systematics of ridge propagation south of 30 degrees s. *Earth and Planetary Science Letters*, 121.
- Oldenburg, D. W., & Brune, J. N. (1972). Ridge transform fault spreading pattern in freezing wax. *Science*, 178, 301-304.
- Oldenburg, D. W., & Brune, J. N. (1975). An explanation for the orthogonality of ocean ridges and transform faults. *Journal of Geophysical Research*, 80, 2575-2585. doi: 10.1029/jb080i017p02575
- Palmer, J., Sempéré, J.-C., Christie, D. M., & Morgan, J. P. (1993). Morphology and tectonics of the australian-antarctic discordance between 123 e and 128 e. *Marine Geophysical Researches*, 15(2), 121-152.
- Seton, M., Müller, R. D., Zahirovic, S., Williams, S., Wright, N. M., Cannon, J., ... McGirr, R. (2020). A global data set of present-day oceanic crustal age and seafloor spreading parameters. *Geochemistry, Geophysics, Geosystems*, 21, 1-15. doi: 10.1029/2020GC009214
- Shi, P., Wei, M. M., & Pockalny, R. A. (2022). The ubiquitous creeping segments on oceanic transform faults. *Geology*, 50, 199-204. doi: 10.1130/G49562.1
- Tozer, B., & Sandwell, D. T. (2019, 8). *Tozer et al., (2019) SRTM15+ GMT Grids*. Retrieved from [https://figshare.com/articles/online\\_resource/Tozer\\_et\\_al.2019\\_SRTM15\\_GMT\\_Grids/7979780](https://figshare.com/articles/online_resource/Tozer_et_al.2019_SRTM15_GMT_Grids/7979780) doi: 10.6084/m9.figshare.7979780.v2
- Tozer, B., Sandwell, D. T., Smith, W. H., Olson, C., Beale, J. R., & Wessel, P. (2019). Global bathymetry and topography at 15 arc sec: Srtm15+. *Earth and Space Science*, 6, 1847-1864. doi: 10.1029/2019EA000658
- Tucholke, B. E., Lin, J., Kleinrock, M. C., Tivey, M. A., Reed, T. B., Goff, J., & Jaroslow, G. E. (1997). Segmentation and crustal structure of the western mid-atlantic ridge flank, 25deg 25'-27deg 10'n and 0-29 m.y. *Journal of Geophysical Research: Solid Earth*, 102, 10203-10223. doi: 10.1029/96jb03896
- Uieda, L., Tian, D., Leong, W. J., Jones, M., Schlitzer, W., Grund, M., ... Wessel, P. (2022, July). *PyGMT: A Python interface for the Generic Mapping Tools*. Zenodo. Retrieved from <https://doi.org/10.5281/zenodo.6702566> doi: 10.5281/zenodo.6702566
- Wang, T., Tucholke, B. E., & Lin, J. (2015). Spatial and temporal variations in crustal production at the mid-atlantic ridge, 25deg n-27deg 30'n and 0-27ma. *Journal of Geophysical Research: Solid Earth*, 120. doi: 10.1002/2014JB011501
- Watts, A. B. (2001). *Isostasy and flexure of the lithosphere*. Cambridge University Press.
- Wessel, P., Luis, J., Uieda, L., Scharroo, R., Wobbe, F., Smith, W. H., & Tian, D. (2019). The generic mapping tools version 6. *Geochemistry, Geophysics, Geosystems*, 20(11), 5556-5564.
- West, B. P., Lin, J., & Christie, D. M. (1999). Forces driving ridge propagation. *Journal of Geophysical Research: Solid Earth*, 104, 22845-22858. doi: 10.1029/1999jb900154
- Zhang, F., Lin, J., Zhou, Z., Yang, H., & Morgan, J. P. (2022). Mechanism of progressive broad deformation from oceanic transform valley to off-transform faulting and rifting. *The Innovation*, 3. Retrieved from <http://dx.doi.org/10.1016/j.xinn.2021.100193> doi: 10.1016/j.xinn.2021.100193
- Zheng, T., Tucholke, B. E., & Lin, J. (2019). Long-term evolution of nontransform discontinuities at the mid-atlantic ridge, 24n-27 30n. *Journal of Geophysical Research: Solid Earth*, 124, 10023-10055. doi: 10.1029/2019JB017648